ACS APPLIED MATERIALS & INTERFACES

Research Article

www.acsami.org

Simple Growth of Faceted Au–ZnO Hetero-nanostructures on Silicon Substrates (Nanowires and Triangular Nanoflakes): A Shape and Defect Driven Enhanced Photocatalytic Performance under Visible Light

Arnab Ghosh,[†] Puspendu Guha,[†] Aneeya K. Samantara,[‡] Bikash Kumar Jena,[‡] Rajshekhar Bar,[§] Samit Ray,[§] and Parlapalli V. Satyam*,[†]

[†]Institute of Physics, Sachivalaya Marg, Bhubaneswar 751005, India
[‡]CSIR-Institute of Minerals and Materials Technology, Bhubaneswar 751013, India
[§]School of Nano Science & Technology, Indian Institute of Technology, Kharagpur 721302, India

Supporting Information

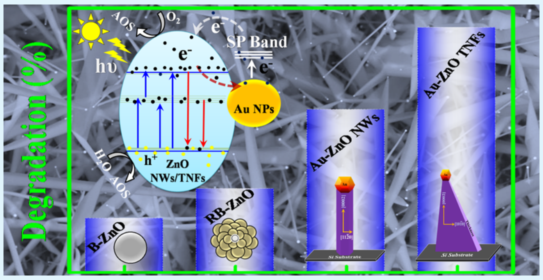

ABSTRACT: A simple single-step chemical vapor deposition (CVD) method has been used to grow the faceted Au–ZnO hetero-nanostructures (HNs) either with nanowires (NWs) or with triangular nanoflakes (TNFs) on crystalline silicon wafers with varying oxygen defect density in ZnO nanostructures. This work reports on the use of these nanostructures *on* substrates for photodegradation of rhodamine B (RhB) dyes and phenol under the visible light illumination. The photoluminescence measurements showed a substantial enhancement in the ratio of defect emission to band-edge emission for TNF (ratio ≈ 7) compared to NW structures (ratio ≤ 0.4), attributed to the presence of more oxygen defects in TNF sample. The TNF structures showed 1 order of magnitude enhancement in photocurrent density and an order of magnitude less charge-transfer resistance (R_{ct}) compared to NWs resulting high-performance photocatalytic activity. The TNFs show enhanced photocatalytic performance compared to NWs. The observed rate constant for RhB degradation with TNF samples is 0.0305 min^{-1}, which is $\approx$5.3 times higher compared to NWs case with 0.0058 min^{-1}. A comparison has been made with bulk ZnO powders and ZnO nanostructures without Au to deduce the effect of plasmonic nanoparticles (Au) and the shape of ZnO in photocatalytic performance. The results reveal the enhanced photocatalytic capability for the triangular nanoflakes of ZnO toward RhB degradation with good reusability that can be attracted for practical applications.

KEYWORDS: *hetero-nanostructures, triangular nanoflakes, oxygen defects, photoelectrochemistry, photocatalyst, dye degradation*

1. INTRODUCTION

Highly ordered and oriented nanoscale metal oxides structures (NSs) in conjunction with plasmonic noble-metal nanoparticles (NPs) have great potential in micro-/nanodevices for electronic, optical, and photocatalytic applications.[1−5] In the past few decades, environmental problems such as air and water pollution have become a major issue for economic development and human health. Semiconductor based photocatalytic reactions have attracted intense interest as an effective candidate for environmental treatments.[6,7] Among several oxide semiconductor photocatalysts, TiO_2 and ZnO have been most exciting materials for detoxification/purification of water/air and degradation of persistent organic pollutants (such as various dyes) present in wastewater through photocatalytic processes.[8−17] In comparison with TiO_2, ZnO has been actively worked upon from a variety of research communities due to their high photosensitivity, large direct bandgap (3.37 eV), relatively high exciton binding energy (60 meV), nontoxic character, abundance in reserve, and low-cost large-scale synthesis viability.[12−15,17−19] Besides the photocatalytic applications of ZnO NSs, they have been extensively used in several functional devices.[20−24] As the size and shape of the NSs have key importance on their applications, various one-dimensional (1-D) ZnO NSs with different morphologies, such as nanowires (NWs), nanorods (NRs), nanotubes (NTs), nanobelts, nanonails, nanoflakes (NFs), nanowalls, nanotetrapods, and nanosheets, have been synthesized.[25−27] To get such variations, several growth/synthesis protocols have been established, such as solution based synthesis, pulsed laser deposition, and vapor phase depositions (such as CVD, MOCVD, and thermal evaporation etc.) with and without catalyst and so forth.[25,27−30] The pure ZnO NSs show the absorption capabilities only in UV light ($\lambda \leq 370$ nm) due to its high bandgap (3.37 eV). This limits the use of ZnO in facile visible light driven photocatalytic

Received: January 21, 2015
Accepted: April 21, 2015
Published: April 21, 2015

DOI: 10.1021/acsami.5b00634
ACS Appl. Mater. Interfaces 2015, 7, 9486−9496

applications in its pure form. So, a lot of effort has already been devoted to extend/improve the visible light absorption capabilities (major part of solar spectrum) of ZnO material by tailoring their size, morphology, surface area, doping of nonmetals, and most importantly defect concentrations related to oxygen (vacancies or interstitials).[12,13,31−38] Among all of the pathways of boosting visible light photocatalysis, creation of oxygen vacancies is one of the convenient methods which not only increases the visible light absorption by narrowing the bandgap but also restrains the recombination processes of photogenerated e^- and h^+ pairs by acting as active trap centers.[12,13,38,39] Though ZnO nanostructures have been studied extensively, our report on the growth of shape and defect controlled Au−ZnO hetero-nanostructures (HNs such as NWs and TNFs) on Si substrates using simple single-step CVD technique with excellent visible light induced photocatalytic properties could be one of the first of such reports.

The hybridization/integration of Au NPs as plasmonic noble metal on the surfaces of metal oxide NSs (such as TiO_2 and ZnO) to form metal−semiconductor HNs have been proposed as a promising way to increase the photocatalytic efficiency.[18,19,40−43] In particular for the Au−ZnO HNs case, Au NPs act as a sink for photogenerated electrons and restrain the recombination processes. The Au NPs contribute a better charge separation process as well as facilitate electron and hole pairs production by their surface plasmon resonance (SPR) property.[18,19,40−42,44−47] Now it is paramount to emphasize that all of the previous reports have adopted various postgrowth multistep processes to improve photocatalytic activity under visible illumination. In this work, we demonstrate a simple single-step CVD technique that resulted in growth of Au−ZnO nanowires (NWs) and triangular nanoflakes (TNFs), along with significant oxygen defects leading to their efficient visible light photocatalytic application. The use of these structures has been validated by their photoresponse and photocatalytic performance toward degradation of rhodamine B (RhB) and phenol under visible light illumination. To the best of our knowledge, there are no such reports where the growth process of getting hetero-nanostructures with significant oxygen defects in a single-step process and their corresponding visible light activities were systematically studied.

2. EXPERIMENTAL SECTION

2.1. Structural and Optical Characterization. Large-scale single-crystalline nanostructures of the Au−ZnO system (NWs and TNFs) were grown by keeping the substrates at two different positions (downstream and upstream) in a single-zone, side entry quartz tube furnace as depicted in Figure 1. One side of the quartz tube was connected to the gas inlet controlled by a mass flow controller, and the other side had the gas outlet. Initially ≈5 nm thick Au films were deposited (using high-vacuum coating methods) on Si(110) substrates (that has ≈2 nm of SiO_x (native oxide)) and annealed at 800 °C for 30 min in air prior to growth of Au−ZnO HN arrays. Annealing of Au films on native oxide covered silicon substrates yielded well oriented and dispersed gold nanoparticles on silicon substrates, and such a procedure is known as solid state dewetting.[48] Average diameter and areal density of the Au NPs formed after air annealing are calculated to be 48 ± 6 nm and 3.18×10^{10} NPs·cm^{-2}, respectively. These substrates have been used for the growth of Au−ZnO HNs at a growth temperature of 900 °C for 90 min growth time. In this growth process, a mixture of ZnO (99.999%) and graphite powders (99.999%) at a 1:1 molar ratio was taken as the evaporating source. The source was put at the center of a ceramic boat, and two Au nanoparticles decorated Si(110) substrates were placed ≈2.5 cm away on either side of the source. The as-prepared Au−ZnO NWs (downstream substrate) and TNFs (upstream substrate) samples are hereafter referred as samples A and B, respectively. Argon gas has been used as carrier gas with 30 cm^3(STP) min^{-1} mass flow. All details of the CVD growth experimental conditions have been described in our previous work.[48]

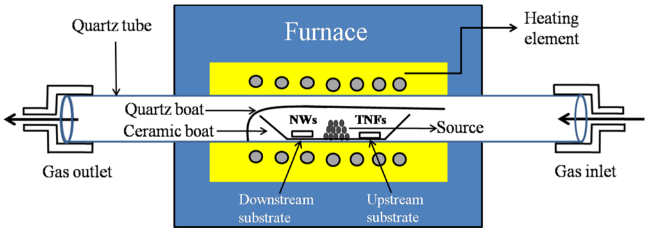

Figure 1. Schematic illustration of the single-zone horizontal tube furnace system for the growth of Au−ZnO hetero-nanostructure (nanowire and triangular nanoflakes) arrays at 900 °C under 30 cm^3(STP) min^{-1}Ar gas flow.

Surface morphology, shape, and size of the as-grown Au−ZnO NWs and TNFs arrays were examined using field emission gun based scanning electron microscopy (FEG-SEM) equipped with BSE detector, with 20 kV electrons (Neon 40 cross-beam system, M/S Carl Zeiss GmbH) and high-resolution transmission electron microscopy (HRTEM) with 200 keV electrons (2010, JEOL HRTEM). Detailed structural analysis was performed using HRTEM with selected area electron diffraction (SAED) pattern capabilities. For HRTEM investigations, the Au−ZnO NWs and TNFs first mechanically scratched from respective samples and then dispersed on two different carbon coated Cu grids by drop-casting. The local compositional analyses of HNs were done by energy dispersive X-ray (EDX) spectrum that is coupled with SEM. X-ray diffraction (XRD) measurements were performed by a Philips Xpert PRO MRD Cradle using Cu Kα ($\lambda = 1.54$ Å) radiation. Optical properties of the samples were characterized by photoluminescence (PL) setup under the excitation of a He−Cd laser (325 nm pump line) at room temperature. Cathodoluminescence (CL) or electron beam induced radiation emission (EIRE) spectroscopy was performed in a ZEISS SUPRA40 SEM equipped with the Gatan MonoCL3 cathodoluminescence system. The X-ray photoelectron spectroscopy (XPS) measurements were carried out using VG Scienta hemispherical analyzer having resolution of 44.1 meV at 50 pass energy and Al Kα ($h\nu = 1486.6$ eV) source (S/N:10001, Prevac, Poland).

2.2. Photoelectrochemical Measurements. For photoelectrochemical measurements, powders from sample A and sample B were scraped off and dispersed on indium tin oxide (ITO) coated quartz substrate and dried prior use. These two types of Au−ZnO HNs (NWs and TNFs) modified ITO/quartz were used as the working electrode. The photoelectric response measurements were carried out by illuminating 1 cm^2 of the working electrode at zero bias voltage against Ag/AgCl reference electrode in 0.01 M Na_2SO_4 as the supporting electrolyte. Here, the photoresponse spectra were obtained with a 100 W lamp (with a luminous irradiance of 10 mW/cm^2 at the sample) with switch ON and OFF conditions, and the generated photocurrent signals were measured by the CHI 660C electrochemical workstation.

2.3. Photocatalytic Activity. The photocatalytic activity of the as-grown HNs samples (samples A and B) were evaluated by degradation of rhodamine B (RhB) and phenol (as standard organic pollutant) in aqueous solution under visible light irradiation. For both the cases, NWs and TNFs coated Si substrates of area 0.5 cm^2 were immersed in a 10 mL RhB solution (5×10^{-6} M) under the illumination of a 100 W bulb (with a luminous irradiance of 10 mW/cm^2 at the sample) with continuous stirring in a beaker. Before the light was switched on, the beaker containing photocatalyst and RhB solution was stirred in the dark for 30 min to ensure an equilibrium adsorption of dye molecules on the catalyst Au−ZnO NWs or TNFs on Si surfaces. Subsequently, at regular intervals from 30 min to 3 h of exposure, 4 mL solutions were withdrawn for monitoring absorption changes using a UV−vis absorption spectroscopy (Shimadzu UV-2600). The RhB residual concentration was determined by checking the changes in the absorbance maximized at λ_{max}= 554 nm as a function of irradiation time. For the phenol (5×10^{-6} M) degradation study, all of the experimental conditions remained the same as those in the RhB case, and the residual concentration was determined by following the changes in the absorbance maximized at λ_{max}= 270 nm as a function of irradiation time.

3. RESULTS AND DISCUSSION

3.1. Morphological and Structural Characterization.

The morphological studies were carried out with FE-SEM (both secondary electron (SE) and backscattered electron (BSE) images) for both samples A and B. Parts a and c of Figure 2 depict low-magnification SE images for sample A and sample B, respectively. The insets of these panels in Figure 2 clearly show nanowire and triangular nanoflake structures with faceted Au nanostructures at the apex. High-magnification backscattered electrons (BSE) images taken for sample A (downstream) and sample B (upstream) have been shown in Figures 2b,d, wherein the brighter contrasts correspond to Au NPs for both samples. Low-magnification BSE images of samples A and B are shown in the Supporting Information (SI) (Figures S1a,b). It shows an abundance of ZnO nanostructures. Typically, sample A consists of Au−ZnO NWs with uniform diameter hexagonal cross-sections, but in sample B, the majority of the HNs are TNFs having rectangular cross-sections with very little amount of NWs being observed. The cross-sectional view of the samples is shown in SI Figures S1c,d. This reveals that the Au−ZnO NWs as well as TNFs are randomly aligned. Statistical observations on respective samples have been summarized in Table 1.

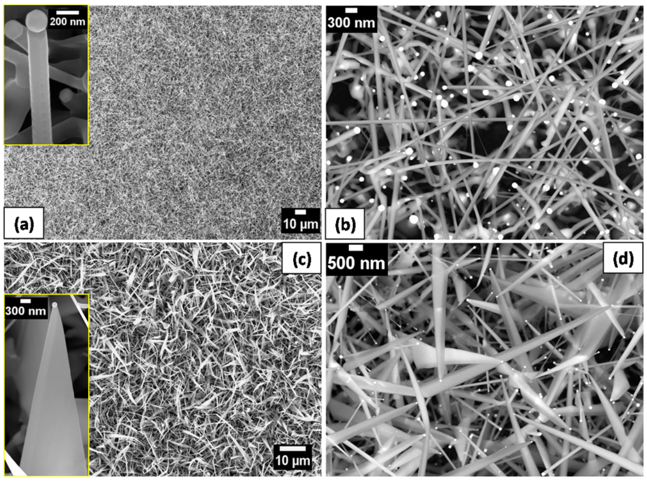

Figure 2. SEM micrographs of as-grown Au-ZnO hetero-nanostructures (nanowires and triangular nanoflakes) on 5 nm Au/SiO_2/Si(110) preannealed at 800 °C with substrates kept at two different positions (down stream and up stream of CVD system): (a and c) top views low-magnification secondary electron images of sample A (NWs) and sample B (TNFs), respectively; (b and d) corresponding samples' high-magnification backscattered electron images. Inset of panels a and c show the SE images of a single NW and TNF, respectively.

The results show that the substrate's position is a critical growth parameter for the growth of 1-D Au−ZnO HNs of different morphologies. Elemental analyses of the as-grown samples were done using energy dispersive spectrometry (EDS) equipped with FE-SEM and are shown in SI Figure S2. The EDS spectra from both of the HNs indicate that faceted NPs at their tip are having Au as a major contribution with a smaller amount of Zn, whereas their body parts show only O and Zn signals.

Table 1. Detail about the Dimensions and Areal Densities of the As-Grown Samples

details	sample A (NWs)	sample B (TNFs)
tip diameter (nm)	130 ± 40	112 ± 49
length (μm)	6 ± 5	8 ± 6
base (nm)	130 ± 40	1500 ± 700
areal density (NSs/cm^2)	4.27×10^8	4.0×10^8
cross-section along the growth direction	uniform hexagonal	gradually tapered rectangular

Detailed structural studies on Au−ZnO NWs and TNFs were further carried out using TEM with SAED and HRTEM. Parts a and d of Figure 3 show the low-magnification TEM micrographs of a single Au−ZnO NW and TNF, respectively, and reveal a faceted Au NP at the apex of each of them. The corresponding HRTEM images are shown in Figure 3b,e from the highlighted regions of Figure 3a,d, suggesting that Au−ZnO HNs are grown along the [0001] crystal direction (*c*-axis oriented). SAED patterns from the Au−ZnO NWs and TNFs bodies were taken along the $[1\bar{1}00]$ and $[1\bar{2}10]$ zone axes and are shown in Figure 3c,f, respectively. These show the single-crystalline nature with hexagonal wurtzite phase of the HNs grown along the common [0001] direction. We have also done XRD analysis on both samples to check the large-scale crystalline information. XRD results shown in SI Figure S3a,b further confirm the single-crystalline nature of the HNs in samples A and B, respectively, besides the TEM and SAED observations.

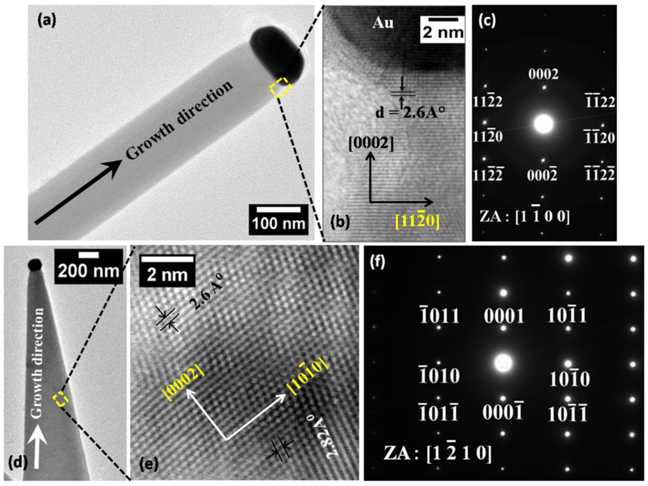

Figure 3. (a and d) Low-magnification TEM micrographs of individual ZnO NW and TNF with faceted Au particle at their tip, respectively; (b) HRTEM image of the highlighted area in panel a; (e) HRTEM image taken from the TNF body in panel d; (c and f) selected area diffraction (SAED) patterns from individual NW and TNF, respectively.

The growth fronts of each of the NW and TNF terminated with faceted catalyst Au NPs, confirmed by TEM, HR-SEM, and EDS, suggest that both are catalyst assisted growth.[28−30,49,50] The growth of faceted NWs are in uniform diameter. But a gradual shrinking of diameter toward the

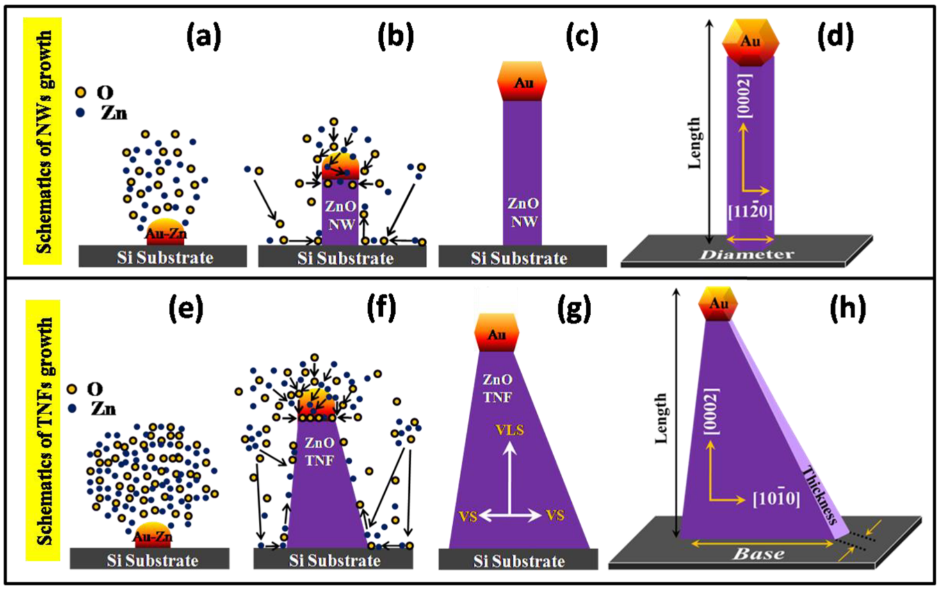

Figure 4. Schematic illustrations showing the possible growth model for a Au capped ZnO nanowire (NW) (a−c) and triangular nanoflakes (TNF) (e−g); (d and h) three-dimensional geometrical configuration of a fully grown NW and TNF, respectively.

growth direction of faceted TNFs was observed. The presence of catalyst NP at the tip and the faceted side wall of HNs suggest that the growth mechanism is a mixture of VLS and VS processes.[29,30,50,51] The influences of substrate position over differences in Au−ZnO HNs morphology are discussed thoroughly in the proposed growth models.

3.2. Proposed Growth Models. In this present work, for both cases we have found the catalyst NPs at the tip of the HNs (NWs and TNFs) confirm the VLS growth mode and this is also supported by other experimental observations, which is quite consistent with previous reports.[28−30,49,50,52] The VLS mechanism involves the supply of growth species (Zn and O) through carbothermal reactions to the catalyst droplet on Si, beyond their solubility limits, leads to precipitation (after supersaturation is reached) at the interface of Au−Zn alloy droplet and Si substrate. Further oxidation by the O molecule around the substrate results in nucleation of Au−ZnO HNs.[48] However, owing to faceted side walls with a uniform hexagonal cross-section of NWs (sample A) and triangular morphology of the TNFs (sample B) with rectangular cross-section, it is not a conventional VLS process which alone is responsible for these growths. Rather this growth is a combination of two processes: (1) catalyst assisted VLS growth responsible for faster axial growth and (2) catalyst free VS growth which governs the radial growth of side walls.[29,30,50,51] It is obvious that the catalyst driven axial growth rate beneath the catalyst droplet and interface of Au−ZnO will be much faster compared to catalyst free side-wall growth of nonpolar faces, due to the polar nature of ZnO as well as a strong binding affinity of Au atoms to its polar faces.[30,50,51,53]

The growth mechanism of Au−ZnO NWs (sample A) in this case is somewhat similar to that reported by Weigand et al. where nucleation is initiated by catalyst droplet through VLS mechanism along with simultaneous side-wall deposition via VS mechanism.[30] Even though the growth rate is higher at the interface of catalyst NW, still specific growth environments can facilitate significant side-wall growth via VS mechanism with growth rate governed by the availability of growth species and the surface free energy of the exposed surfaces.[30,54] The radial growth rate will be isotropic for NWs (sample A) as the side walls are enclosed by six identical $\{11\bar{2}2\}$ facets with equal surface free energies and VS growth rates, leading to the formation of uniform diameter of hexagonal cross-section NWs. The proposed growth model for Au−ZnO NWs growth at the downstream substrate has been illustrated schematically in Figure 4a−d. On the other hand, for the substrate kept at the upstream location (sample B), the majority of the ZnO NSs consist of nanoflakes with triangular-like morphology (TNFs) with faceted Au NPs at the tip headed upward. In the past, several ways have been adopted to explain the origin of tapered morphology of the NSs, which includes catalyst droplet instability (due to the high growth temperature and high gas flow rate and pressure) and/or oversupply of growth species to the catalyst droplets serve as active consumption sites.[55,56] In our experiment, at the same time we have grown HNs (NWs and TNFs) of two different morphologies on the two similar substrates kept at two different positions. The substrate position appears to be the major reason for these two kinds of HNs. As sample B (upstream substrate) was placed near to the gas inlet end side of the assembly (Figure 1), more supply of growth species (carbothermal reaction produced Zn and O atom) must be there compared to the downstream substrate (sample A) throughout the growth process. Detailed justification for the availability of growth species more on the upstream substrate compared to the downstream substrate is discussed in the Supporting Information (Figure S4). The average surface area (ASA) of TNFs is $\sim$8 times higher than that for NWs ($\mathrm{TNF_{ASA}/NW_{ASA}} \approx 8$). As the TNFs become narrow along the growth direction from a wider base, most probably the VLS model controls the axial growth, while the VS growth process controls the radial growth. Here also nucleation started at the catalyst−TNF interface, similar to that of the NWs case with the predominant catalyst assisted axial growth rate. However, in this case particularly due to the oversupply of growth species, the VS growth rate is higher and highly anisotropic compared to NWs growth case leading to the growth of triangular morphology NSs. A wider base with sharp tip end morphology may be arise due to the fact that the VS

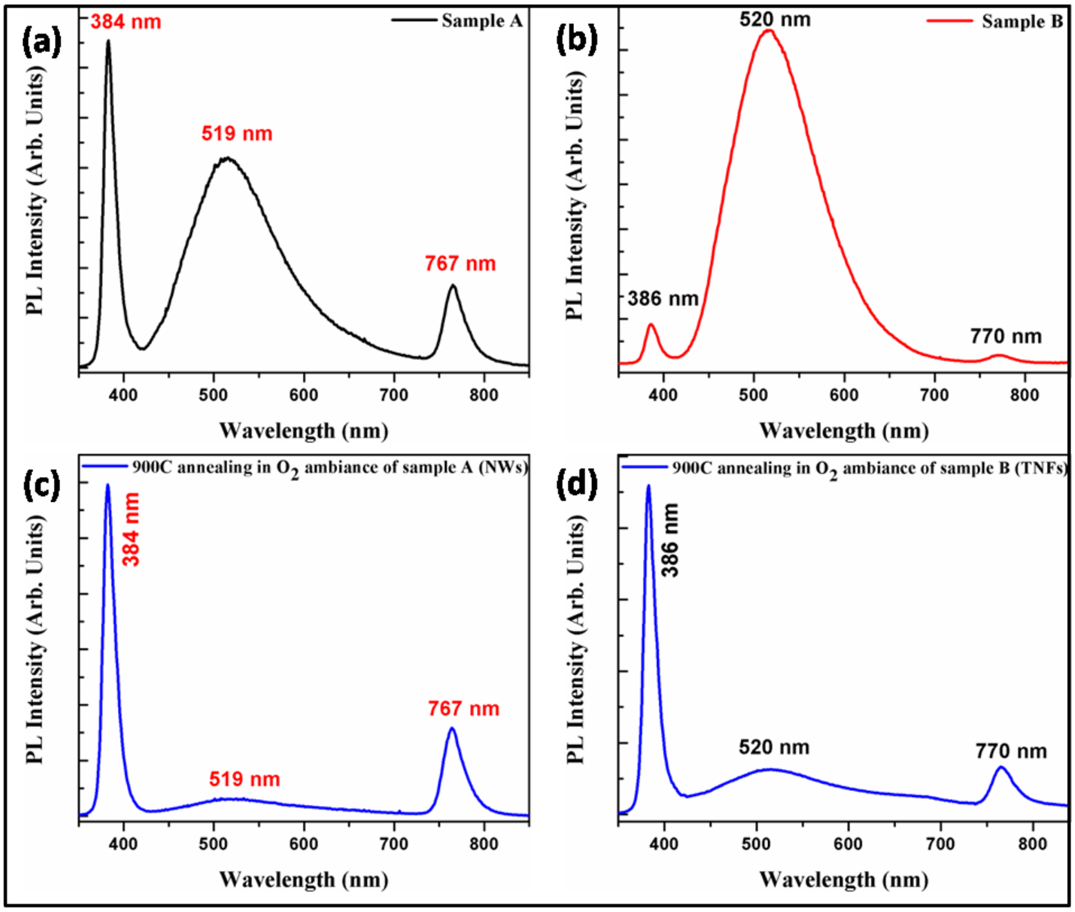

Figure 5. (a and b) Room temperature (300° K) PL spectra taken from sample A (Au−ZnO NWs) and sample B (Au−ZnO TNFs), respectively; (c and d) PL spectra after annealing in an oxygen environment of the corresponding samples at 900 °C for 90 min.

growth rate is increasing toward the base because catalyst Au NP present at the tip of the HNs promotes faster VLS growth rate. Even though ZnO $\{10\bar{1}0\}$ facets are the most stable surfaces from the surface energy point of view,[27,57] still we are getting significant catalyst free radial growth via the VS process along these facets for sample B. This experimental observation can be attributed to preferred VS growth along higher Miller indices and lower specific surface energy planes $\{10\bar{1}0\}$ promoted by our specific growth environments. It has been previously observed that Au−ZnO HNs growth direction and radial growth rate via VS mechanism can be greatly influenced by growth conditions and atmosphere (such as temperature, O_2 partial pressure, gas flow rate, substrate, and choice of catalyst etc.).[26,27,30] Based on this experimental evidence, growth of TNFs at the upstream substrate has been illustrated schematically in Figure 4e−h. However, detailed understanding behind this growth of ZnO TNFs is not very clear to us at this stage.

Since the nucleation of the HNs (NWs and TNFs) were initiated by the catalyst Au NPs on respective Si substrates and the diameter of the NSs are comparable to the size of Au NP, there is a choice of controlling their dimension as well as growth positions using our growth technique. The reproducible control over the size, shape, and morphology of such HNs on various special substrates would be very challenging for their potential applications.

3.3. Photoluminescence Study. Optical measurements of our as-grown samples were carried out using PL at room temperature. Parts a and b of Figure 5 report the PL spectra taken from samples A and B, respectively, showing three distinct regions of emission (UV, visible, and near-infrared). PL spectra of both samples A and B composed of strong ultraviolet (UV) emission peaks centered at 384 and 386 nm, broad deep-level defect related green emissions (∼519 nm/2.39 eV and ∼520 nm/2.38 eV) along with sharp near-infrared peaks around 767 and 770 nm, respectively. Near-band-edge (NBE) UV emission is attributed to the neutral donor bound exciton (NDBE) recombination.[58,59] It is important to emphasize that the intensity of the green emission band from sample B is almost seven times the intensity of its NBE whereas for sample A the intensity of the green emission is almost half of its NBE. Several reports are there explaining the various origins of the defect induced visible luminescence depending on the growth temperature, growth substrate, ambiance, precursor, and choices of catalyst.[58,60,61] To check whether oxygen related defects are causing this visible emission or not, we have performed annealing experiments under oxygen environment for both the as-grown samples at ∼900 °C for 90 min. The PL spectra of these oxygen annealed samples are shown in Figure 5c,d. We have seen from the PL spectra taken on both oxygen annealed samples that the green emissions intensities have been suppressed significantly. So, the origin of the green light emission can be assigned to the recombination centers created due the presence of oxygen vacancies and interstitials in the interior as well as on the surface of the ZnO NSs.[60−62] The high-intensity green emission band in the PL spectra of TNFs (sample B) compared to NWs (sample A) (Figure 5a,b)

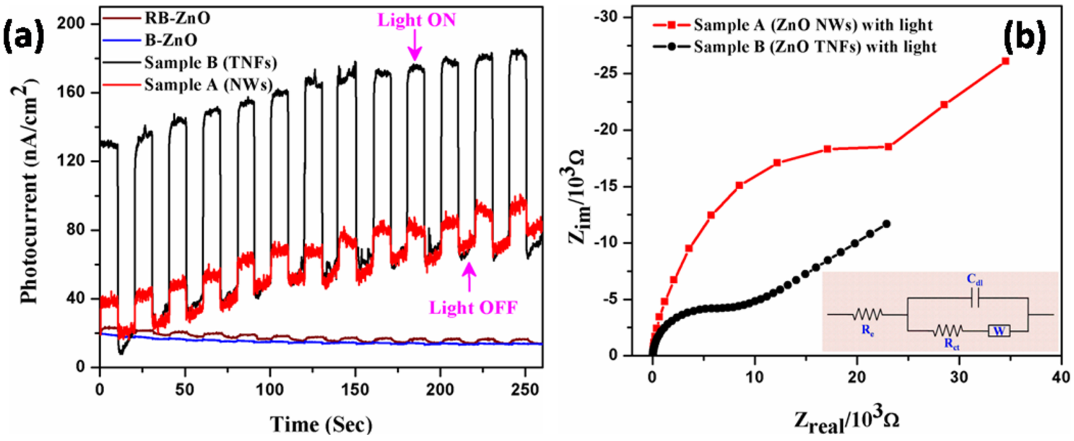

Figure 6. (a) Photocurrent response of sample A and sample B along with B−ZnO and RB−ZnO modified ITO electrode under the periodic irradiation of visible light; (b) Nyquist plots of samples A and B under visible light illumination (inset, corresponding equivalent circuit).

attribute its higher oxygen vacancies. The NBE emission intensity is noticed to be lower than that of the green emission from ZnO TNF (sample B) contrary to the ZnO NW (sample A) case and corroborates that the density of bound excitonic states is lesser than that of oxygen vacancy states.[48,58] One possible reason would be the difference in exposed ASA for the two types of NSs ($TNF_{ASA}/NW_{ASA} \approx 8$). Moreover, a little red shift in the NBE emission position (~386 nm) of TNF (sample B) compared to that of the NW (sample A) case (~384 nm) is found. This behavior may be due to the effect of bandgap narrowing, resulting from a very high amount of oxygen vacancy states in TNFs driving themselves more delocalized and overlapped with the valence band edge.[12,13] An additional peak for both types of ZnO NSs (NWs and TNFs) appears in the near-infrared (near-IR) region centered at 767 and 770 nm, respectively. Because the wavelengths of near-IR emission peaks are approximately twice that (or half in energy scale) of their corresponding NBE emission peaks, thus they could be attributed to the second-order diffraction of NBE emission.[48,63,64] It is also confirmed that luminescence characteristics of individual Au−ZnO HNs for both samples (NWs and TNFs) using high spatial resolution CL measurements are similar to that of PL results (SI Figure S5). To shed more light on the oxygen defect related information, we have carried out XPS measurements on the same as-grown samples shown in SI Figure S6a,b respectively for samples A and B. XPS results further compliment the PL and CL information, indicating that the Au−ZnO TNF sample (sample B) contains more oxygen vacancy related defects compared to the NW sample (sample A).[65]

3.4. Photoelectrochemical Analysis. To evaluate photocatalytic properties of both samples A and B, the photoelectrochemical measurements were performed under visible light ($\lambda \geq 400$ nm) irradiation and compared with bulk ZnO powder (B-ZnO) and chemically synthesized ZnO nanostructures (RB-ZnO)[66] as shown in Figure 6a. The photocurrent response data were collected for both samples under on−off illumination mode. Sample B shows a very high photocurrent density compared to sample A, RB-ZnO and B-ZnO. It is worth pointing out here that the ZnO has a wide band gap and it should not show any photoresponse in visible light in its pure form. Interestingly, the photocurrent response of B-ZnO and RB-ZnO is very low compared to samples A and B suggesting their incapability for absorption of visible light (Figure 6a). However, the enhanced photocurrent response reveals the significant photoabsorption capabilities of samples A and B in visible light. There could be two important possible reasons behind this observation; presence of (a) high midenergy (inside bandgap) oxygen vacancy defect states and (b) visible range plasmonic faceted Au NPs at each and every tip of the NWs and TNFs.[12,13,38,65] The presence of oxygen vacancy in the two different samples are different, complemented by PL, CL, and XPS measurements (vide supra). To support our findings, we also have done diffuse-reflectance analysis. SI Figure S7a shows that in the visible spectrum (400−750 nm) both samples A and B have very broad reflectance minima along with band-edge absorption in the UV regime, which are different from minima (~550 nm with fwhm ~159 nm) due to SPR of Au NPs decorated on standard ZnO substrate shown in SI Figure S7b. So, we can conclude that midenergy defect states as well as plasmonic Au NPs present in both samples A and B contribute together to the visible light absorption. It is also important to note that sample B (TNFs) has smaller reflectance compared to sample A (NWs), indicating the presence of more oxygen vacancy defect states in sample B (SI Figure S7a). Interestingly, the observed photocurrent density distinguishes their photoresponse and sample B shows a significantly higher level than that of sample A. This can be attributed due to the enhanced transfer of photoexcited electrons from the valence band (VB) of ZnO and SPR of Au NPs to the conduction band (CB) of ZnO.[47] Because both samples contain almost the same density of Au−ZnO HNs (NWs and TNFs), so the difference in their photoresponse must be coming from the variation of their O vacancy concentrations. From PL analysis, it is clear that sample B has more oxygen vacancy with respect to sample A, facilitating a high order of charge separation and electron-transfer efficiency of the e^- and h^+ pairs leading to better photoresponse performances. To gain deeper insight into the electron transport behaviors in the photoanode, the electron-transfer process of the samples has been investigated by electrochemical impedance (EI) study. Figure 6b shows the Nyquist plots for samples A and B in the presence of visible light. The charge-transfer resistance (R_{ct}) of the samples is estimated from the diameter of the arc in the Nyquist diagram. The smaller R_{ct} value represents better charge-transfer ability.[67,68] Therefore, the electrochemical impendence spectral data are fitted using a suitable equivalent circuit diagram to calculate the R_{ct} values. It denotes that the R_{ct} of sample A (~60

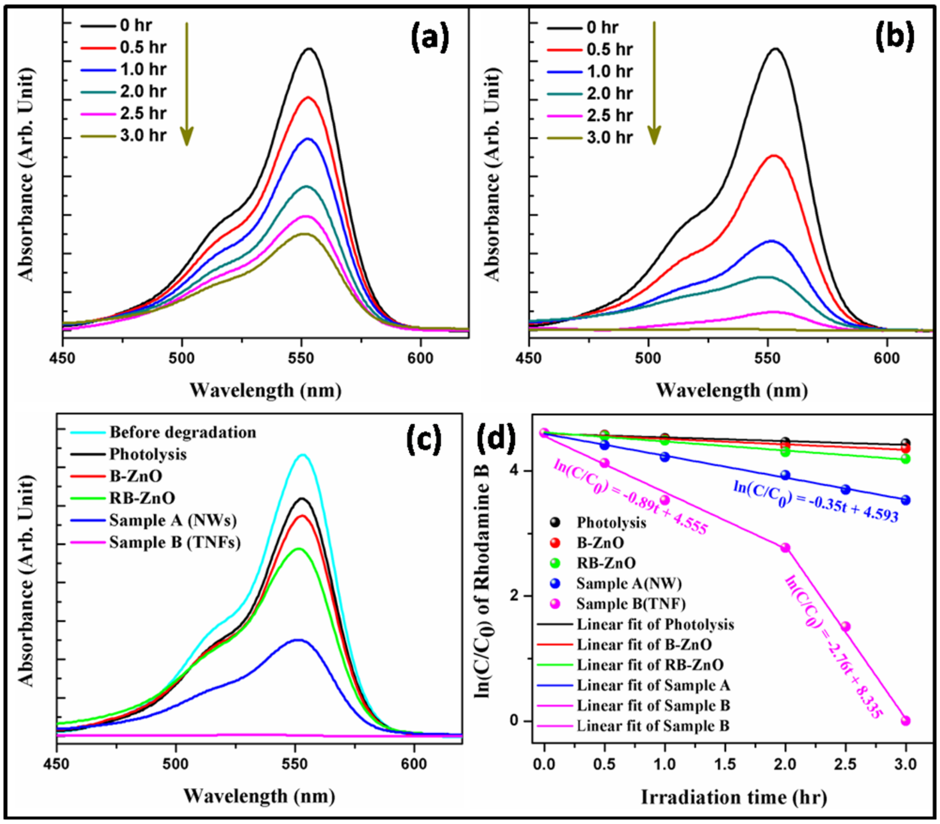

Figure 7. UV−visible absorption spectra of 5 μM RhB in the presence of (a) sample A and (b) sample B under visible light irradiation at different time intervals; (c) UV−visible spectra of RhB before and after treatment with sample A, sample B, B-ZnO, and RB-ZnO and only with light after 3 h of irradiation; (d) first-order kinetics plots [$\ln(C/C_0$, in %) vs irradiation time (t)] of the photocatalytic activities of the as-grown photocatalysts for RhB degradation under visible light.

kΩ) is almost 10 times higher than that of sample B (∼6.6 kΩ). This can be attributed to the presence of more oxygen vacancies in sample B compared to sample A, which actually facilitates the better electron-transfer efficiency on its surfaces.[14,67] In order to support the preceding fact, the EIS measurement was carried out for RB-ZnO for comparison thereof (SI Figure S8). It shows a bigger diameter of the arc in the Nyquist diagram suggesting very high R_{ct} value compared to samples A and B. Because the photocurrent response for B-ZnO was negligible (see Figure 6a), we have not done EIS measurement for this. It is also important to highlight that the oxygen vacancy is not only one factor for visible light absorption of ZnO nanostructures but the Au nanoparticles (NPs) on every ZnO nanostructure play also a crucial role. Because Au NP exhibits a SPR band in the visible range of about λ = 520−560 nm, upon irradiation of visible light electrons below the Fermi level (E_f) will be excited to the surface plasmon (SP) states, leaving positive charges (h^+) below E_f. At the same time e^- from VB and defect states of ZnO NSs will be excited to CB, and further transferred to the Fermi level of Au, because most of the defect levels and E_f of ZnO lie below the E_f of Au.[41,44,46,47,65] In this case, Au NPs act an electron trap sites for the efficient separation of photogenerated e^- and h^+ pairs to increase the photocurrent, along with oxygen vacancy states.

3.5. Photocatalytic Degradation of Rhodamine B.

Inspired by the excellent increased photoelectron-transfer performance of as-synthesized Au−ZnO HNs (samples A and B), the photocatalytic degradation of RhB dye was carried out under visible light irradiation (100 W bulb, with irradiance 10 mW/cm^2 at the sample, $\lambda \geq 400$ nm) to evaluate their photocatalytic performance. Experiments showed that no significant degradation occurred in the absence of either photocatalyst (samples) or light, which confirms that degradation of RhB is a photocatalytic effect of Au−ZnO NWs and TNFs (samples A and B). The temporal evolution of absorption spectra of RhB solution after successive irradiation of light with samples A and B are shown in Figure 7a,b. It was observed that the absorbance maxima of RhB (λ_{max}= 554 nm) markedly decreased with irradiation time and almost vanished after 180 min of irradiation with sample B. The optical photographs of the RhB solution after treatment with sample B at different intervals of time were collected and presented in Figure S9, SI. It is worth emphasizing that the photocatalytic decolorization (or mineralization) of RhB is better for sample B. This can be attributed to the presence of a high concentration of oxygen vacancy states which enhances or facilitates degradation processes.[14,36,67] Further, the photocatalytic performance of B-ZnO and RB-ZnO nanostructures was checked to authenticate the preceding fact. Interestingly, these samples show very less photocatalytic efficiency compared to sample A and sample B (SI Figure S10). Overall, the RhB degradation performances of all of the samples after 3 h of visible light irradiation and the corresponding change in color of RhB are shown in Figure 7c and SI Figure S11, respectively. Figure 7d shows the degradation trends of RhB solution as a function of irradiation time, which clearly shows that the TNFs sample (sample B) has higher photocatalytic activity compared to those of samples A, B-ZnO, and RB-ZnO. Photocatalytic decolorization of low concentration dye followed a pseudo-first-order reaction and its kinetics can be expressed as, $\ln(C/C_0) = -kt$,[10,39,41,42] where k is the apparent rate constant and C_0 and C are the initial and after irradiation concentrations of RhB solution, respectively. The rate constants (k) for RhB degradation were calculated to be 0.0015, 0.0024, 0.0058, and 0.0305 min^{-1} (average of two slopes in two regions 0−2 and 2−3 h with k values of 0.015 and 0.046 min^{-1}) respectively for B-ZnO, RB-ZnO, sample A, and sample B (see Figure 7d). Considering the average wavelength of the visible light (λ = 550 nm), we have calculated the average photonic efficiency (Φ) using the equation

$$\Phi/\% = (kC_0V/I_0A) \times 100$$

where I_0 is the photon flux (einsteins s^{-1} cm^{-2}), k is the degradation rate constant (s^{-1}), A is the illuminated area (cm^2), C_0 is the initial RhB concentration (mol L^{-1}), λ is the average illumination wavelength of the visible light (meter), and V is the volume of RhB aqueous solution (L).[69] The average photonic efficiencies (Φ) for B-ZnO, RB-ZnO, sample A (NWs) and sample B (TNFs) are calculated to be 0.0054%, 0.0085%, 0.021%, and 0.11%, respectively. Thereof sample B (TNFs) over sample A (NWs) appears to be the best photocatalyst among all, toward the degradation of RhB. To verify the enhanced photocatalytic properties of the as-grown sample B (TNFs) compared to sample A (NWs), we have further carried out the degradation of standard organic pollutant phenol in aqueous (5×10^{-6} M) solution under exactly similar experimental conditions (such as RhB degradation). We found from the phenol degradation plots, indeed sample B (TNFs) has superior photocatalytic property than sample A (NWs) shown in SI Figure S12. The photocatalytic stability of as-grown samples was also evaluated to check their reusability upon 3 h of irradiation up to 5 consecutive cycles of photodegradation (of only RhB) experiment (Figure 8). Interestingly, the dye degradation capabilities for both samples A and B remain unchanged without any further treatment even after five cycles of experiments. Further TEM and SAED results from samples A and B after being used for five cycles of degradation performances indicate good stability and recyclability of the as-grown HNs (SI Figure S13). This signifies the excellent efficiency of the present samples for practical applications. The point should be noted here that the present samples will attract better practical photocatalytic applications compared to the available powdered samples (B-ZnO and RB-ZnO powder). The main disadvantage of powder catalysts is the postrecovery tedious process, which barred their commercialization. But the advantage for the photocatalysts grown on the solid substrate is that it can be easily removed from the reaction container, and a simple washing will make it ready for further use.

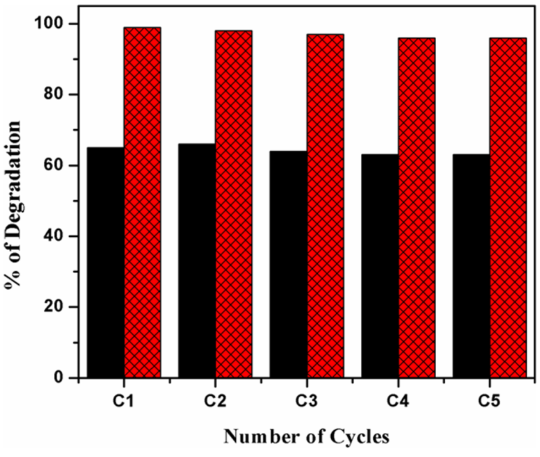

Figure 8. Five cycles for photodegradation of 5 μM RhB by sample A (black) and sample B (red) under visible light irradiation. For each cycle the duration of visible light exposure is 3 h.

3.6. Plausible Photocatalytic Degradation Mechanism. The attempt has been made to discuss the plausible reaction mechanism for the photodegradation of RhB over Au nanoparticle capped oxygen deficient Au−ZnO HNs under visible light irradiation. The reaction mechanism involved during the course of photoassisted degradation of RhB aqueous solution using Au−ZnO HNs as photocatalyst is schematically presented in Figure 9. The photocatalytic activity consists of three competitive processes as follows: (1) generation of e^- and h^+ pairs through absorption of adequate photon energy, (2) charge separation between photogenerated e^- and h^+, and (3) their promotion to the surface of HNs to produce highly active oxidative species (AOS) through surface redox reactions.[70] These strong nonselective oxidants and photoinduced hole (h^+) further react with organic dye RhB and degrade into nontoxic products (e.g., CO_2 and H_2O).[41,70] Usually, the photocatalytic efficiency is limited by the recombination process of photogenerated charge carriers. Here the oxygen vacancy states and plasmonic metal Au NPs together prolong the lifetime of the e^- and h^+ pairs by restraining recombination processes and promote the photocatalytic activity.

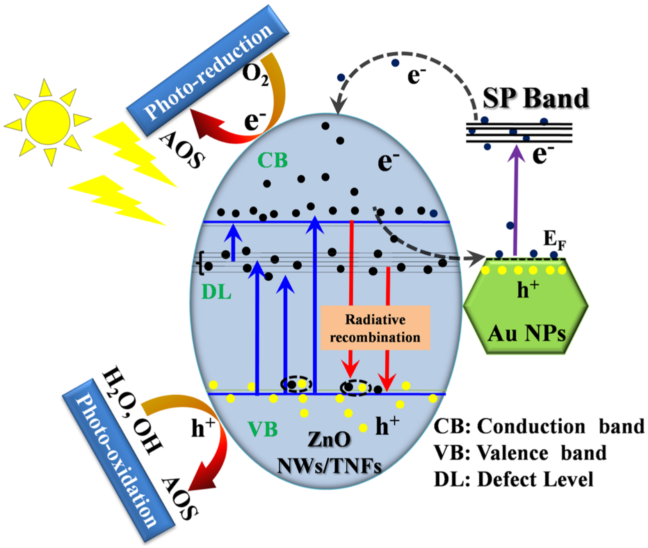

Figure 9. Schematic representation of the possible mechanism behind the photocatalytic activity of as-grown ZnO nanostructures upon degradation of rhodamine B (RhB) induced by visible light ($\lambda \geq 400$ nm).

4. CONCLUSION

In summary, we have grown two different morphologies of Au−ZnO HNs (NWs and TNFs) in a single-step method successfully and discussed the plausible growth mechanisms. From the PL, CL, and XPS measurements, TNF nanostructures are found to have more oxygen related defect states which perhaps are due to a larger average surface area ($TNF_{ASA}/NW_{ASA} \approx 8$) for TNFs compared to NWs. The TNF nanostructures have shown 10 times less charge-transfer resistance (R_{ct}) compared to sample A (NWs) owing to their higher oxygen related defect centers leading to enhancement in visible light induced photocurrent densities (≈4 times). The higher surface defects and less R_{ct} of sample B compared to sample A have delivered better photocatalytic degradation of 5×10^{-6} M RhB with an average degradation rate constant of $0.0305\ min^{-1}$ and photonic efficiency of 0.11%; those are ≈5.3 times higher than those for sample A ($0.0058\ min^{-1}$, 0.021%). We have further cross-checked the enhanced photocatalytic property of sample B over sample A by studying the degradation of standard organic pollutant (phenol). The role of oxygen vacancies in conjunction with the presence of Au NPs at the apex of HNs has been discussed elaborately. Reusability of both samples up to five cycles of operations was checked, showing very good stability and no further treatment is involved before using them in the next cycle. This high photocatalytic property and robustness of the Au−ZnO TNFs sample could endow its use in harnessing the visible part of the solar spectrum toward the degradation of organic compounds and microorganisms in water.

■ ASSOCIATED CONTENT

S Supporting Information

Figures showing some additional backscattered electron images, EDX data, XRD patterns, growth setup schematics, CL spectra, XPS analysis, UV−vis DRS of as-grown HNs (NWs and TNFs), a Nyquist plot of RB-ZnO, temporal color evolution of RhB with TNFs, UV−vis absorption spectra of RhB without catalyst, with B-ZnO, and RB-ZnO, optical photographs of 5 μM RhB aqueous solution and after treatment with all four samples, phenol degradation, and some TEM and SAED data for stability checking and text giving growth explanation and phenol degradation study details. The Supporting Information is available free of charge on the ACS Publications website at DOI: 10.1021/acsami.5b00634.

■ AUTHOR INFORMATION

Corresponding Author

*E-mail: satyam@iopb.es.in; pvsatyam22@gmail.com.

Notes

The authors declare no competing financial interest.

■ ACKNOWLEDGMENTS

P.V.S. thanks the Department of Atomic Energy, Government of India, for 11th Plan Project No. 11-R&D-IOP-5.09-0100 and 12th plan. We also acknowledge Mr. Mohit Kumar (IOP Bhubaneswar) for his help in carrying out UV−vis DRS and XRD measurements.

■ REFERENCES

(1) Kolmakov, A.; Klenov, D. O.; Lilach, Y.; Stemmer, S.; Moskovits, M. Enhanced Gas Sensing by Individual SnO_2 Nanowires and Nanobelts Functionalized with Pd Catalyst Particles. *Nano Lett.* **2005**, *5*, 667−673.

(2) Xie, Y.; Ding, K. L.; Liu, Z. M.; Tao, R. T.; Sun, Z. Y.; Zhang, H. Y.; An, G. M. In Situ Controllable Loading of Ultrafine Noble Metal Particles on Titania. *J. Am. Chem. Soc.* **2009**, *131*, 6648−6649.

(3) Fernandez-Garcia, M.; Martinez-Arias, A.; Hanson, J. C.; Rodriguez, J. A. Nanostructured Oxides in Chemistry: Characterization and Properties. *Chem. Rev.* **2004**, *104*, 4063−4104.

(4) Talapin, D. V.; Lee, J.-S.; Kovalenko, M. V.; Shevchenko, E. V. Prospects of Colloidal Nanocrystals for Electronic and Optoelectronic Applications. *Chem. Rev.* **2009**, *110*, 389−458.

(5) Zheng, Z.; Huang, B.; Qin, X.; Zhang, X.; Dai, Y.; Whangbo, M. H. Facile in Situ Synthesis of Visible-light Plasmonic Photocatalysts M@TiO2 (M = Au, Pt, Ag) and Evaluation of Their Photocatalytic Oxidation of Benzene to Phenol. *J. Mater. Chem.* **2011**, *21*, 9079−9087.

(6) Hoffmann, M. R.; Martin, S. T.; Choi, W.; Bahnemann, D. W. Environmental Applications of Semiconductor Photocatalysis. *Chem. Rev.* **1995**, *95*, 69−96.

(7) Chong, M. N.; Jin, B.; Chow, C. W. K.; Saint, C. Recent Developments in Photocatalytic Water Treatment Technology: A Review. *Water Res.* **2010**, *44*, 2997−3027.

(8) Yu, J. G.; Su, Y. R.; Cheng, B. Template-Free Fabrication and Enhanced Photocatalytic Activity of Hierarchical Macro-/Mesoporous Titania. *Adv. Funct. Mater.* **2007**, *17*, 1984−1990.

(9) Leung, T. Y.; Chan, C. Y.; Hu, C.; Yu, J. C.; Wong, P. K. Photocatalytic Disinfection of Marine Bacteria using Fluorescent Light. *Water Res.* **2008**, *42*, 4827−4837.

(10) Kim, C. W.; Pal, U.; Park, S.; Kim, Y. H.; Kim, J.; Kang, Y. S. Crystallization Induced Porosity Control and Photocatalytic Activity of Ordered Mesoporous TiO_2. *RSC Adv.* **2012**, *2*, 11969−11975.

(11) Liu, G.; Wang, L. Z.; Yang, H. G.; Cheng, H. M.; Lu, G. Q. Titania-Based Photocatalysts-Crystal Growth, Doping and Heterostructuring. *J. Mater. Chem.* **2010**, *20*, 831−843.

(12) Ansari, S. A.; Khan, M. M.; Kalathil, S.; Nisar, A.; Lee, J.; Cho, M. H. Oxygen Vacancy Induced Band Gap Narrowing of ZnO Nanostructures by an Electrochemically Active Biofilm. *Nanoscale* **2013**, *5*, 9238−9246.

(13) Wang, J.; Wang, Z.; Huang, B.; Ma, Y.; Liu, Y.; Qin, X. Oxygen Vacancy Induced Band-Gap Narrowing and Enhanced Visible Light Photocatalytic Activity of ZnO. *ACS Appl. Mater. Interfaces* **2012**, *4*, 4024−4030.

(14) Daneshvar, N.; Salari, D.; Khataee, A. R. Photocatalytic Degradation of Azo Dye Acid Red 14 in Water on ZnO as an Alternative Catalyst to TiO_2. *J. Photochem. Photobiol., A* **2004**, *162*, 317−322.

(15) Sakthivel, S.; Neppolian, B.; Shankar, M. V.; Arabindoo, B.; Palanichamy, M.; Murugesan, V. Solar Photocatalytic Degradation of Azo Dye: Comparison of Photocatalytic Efficiency of ZnO and TiO_2. *Sol. Energy Mater. Sol. Cells* **2003**, *77*, 65−82.

(16) Pal, M.; Pal, U.; Gonzalez, R. S.; Mora, E. S.; Santiago, P. Synthesis and Photocatalytic Activity of Yb Doped TiO_2 Nanoparticles under Visible Light. *J. Nano Res.* **2009**, *5*, 193−200.

(17) Yang, J. L.; An, S. J.; Park, W. I.; Yi, G. C.; Choi, W. Photocatalysis Using ZnO Thin Films and Nanoneedles Grown by Metal-Organic Chemical Vapor Deposition. *Adv. Mater.* **2004**, *16*, 1661−1664.

(18) He, W.; Kim, H.-K.; Wamer, W. G.; Melka, D.; Callahan, J. H.; Yin, J.-J. Photogenerated Charge Carriers and Reactive Oxygen Species in ZnO/Au Hybrid Nanostructures with Enhanced Photocatalytic and Antibacterial Activity. *J. Am. Chem. Soc.* **2014**, *136*, 750−757.

(19) He, W.; Wu, H.; Wamer, W. G.; Kim, H.-K.; Zheng, J.; Jia, H.; Zheng, Z.; Yin, J.-J. Unraveling the Enhanced Photocatalytic Activity and Phototoxicity of ZnO/Metal Hybrid Nanostructures from Generation of Reactive Oxygen Species and Charge Carriers. *ACS Appl. Mater. Interfaces* **2014**, *6*, 15527−15535.

(20) Service, R. F. Materials Science: Will UV Lasers Beat the Blues? *Science* **1997**, *276*, 895.

(21) Huang, M. H.; Mao, S.; Feick, H.; Yan, H. Q.; Wu, Y. Y.; Kind, H.; Weber, E.; Russo, R.; Yang, P. D. Room-Temperature Ultraviolet Nanowire Nanolasers. *Science* **2001**, *292*, 1897−1899.

(22) Lee, C. J.; Lee, T. J.; Lyu, S. C.; Zhang, Y.; Ruh, H.; Lee, H. J. Field Emission from Well-Aligned Zinc Oxide Nanowires Grown at Low Temperature. *Appl. Phys. Lett.* **2002**, *81*, 3648−3650.

(23) Wang, Z. L.; Song, J. H. Piezoelectric Nanogenerators Based on Zinc Oxide Nanowire Arrays. *Science* **2006**, *312*, 242−246.

(24) Cui, Y.; Wei, Q.; Park, H.; Lieber, C. M. Nanowire Nanosensors for Highly Sensitive and Selective Detection of Biological and Chemical Species. *Science* **2001**, *293*, 1289−1292.

(25) Wang, Z. L. New Family of Nanostructures Bright Future for ZnO at the Frontier of Transparent Oxides. *Mater. Today* **2004**, *7*, 26−33.

(26) Gao, P. X.; Wang, Z. L. Nanoarchitectures of Semiconducting and Piezoelectric Zinc Oxide. *J. Appl. Phys.* **2005**, *97*, No. 044304.

(27) Wang, Z. L. Zinc Oxide Nanostructures: Growth, Properties and Applications. *J. Phys.: Condens. Matter* **2004**, *16*, R829−R858.

(28) Yang, P.; Yan, H.; Mao, S.; Russo, R.; Johnson, J.; Saykally, R.; Morris, N.; Pham, J.; He, R.; Choi, H. J. Controlled Growth of ZnO Nanowires and Their Optical Properties. *Adv. Funct. Mater.* **2002**, *12*, 323−331.

(29) Sallet, V.; Sartl, C.; Vilar, C.; Lusson, A.; Galtier, P. Opposite Crystal Polarities Observed in Spontaneous and Vapor-Liquid-Solid Grown ZnO Nanowires. *Appl. Phys. Lett.* **2013**, *102*, No. 182103.

(30) Weigand, C. C.; Bergren, M. R.; Ladam, C.; Tveit, J.; Holmestad, R.; Vullum, P. E.; Walmsley, J. C.; Dahl, O.; Furtak, T. E.; Collins, R. T.; Grepstad, J.; Weman, H. Formation of ZnO Nanosheets Grown by Catalyst-Assisted Pulsed Laser Deposition. *Cryst. Growth Des.* **2011**, *11*, 5298−5304.

(31) Guo, M. Y.; Ng, A. M. C.; Liu, F. Z.; Djurisic, A. B.; Chan, W. K.; Su, H. M.; Wong, K. S. Effect of Native Defects on Photocatalytic Properties of ZnO. *J. Phys. Chem. C* **2011**, *115*, 11095−11101.

(32) Becker, J.; Raghupathi, K. R.; St. Pierre, J.; Zhao, D.; Koodali, R. T. Tuning of the Crystallite and Particle Sizes of ZnO Nanocrystalline Materials in Solvothermal Synthesis and Their Photocatalytic Activity for Dye Degradation. *J. Phys. Chem. C* **2011**, *115*, 13844−13850.

(33) McLaren, A.; Valdes-Solis, T.; Li, G.; Tsang, S. C. Shape and Size Effects of ZnO Nanocrystals on Photocatalytic Activity. *J. Am. Chem. Soc.* **2009**, *131*, 12540−12541.

(34) Jang, E. S.; Won, J. H.; Hwang, S. J.; Choy, J. H. Fine Tuning of the Face Orientation of ZnO Crystals to Optimize Their Photocatalytic Activity. *Adv. Mater.* **2006**, *18*, 3309−3312.

(35) Tian, Z. R.; Voigt, J. A.; Liu, J.; Mckenzie, B.; Mcdermott, M. J.; Rodriguez, M. A.; Konishi, H.; Xu, H. Complex and Oriented ZnO Nanostructures. *Nat. Mater.* **2003**, *2*, 821−826.

(36) Han, Z.; Liao, L.; Wu, Y.; Pana, H.; Shen, S.; Chen, J. Synthesis and Photocatalytic Application of Oriented Hierarchical ZnO Flower-Rod Architectures. *J. Hazard. Mater.* **2012**, *217*, 100−106.

(37) Wang, J. C.; Liu, P.; Fu, X. Z.; Li, Z. H.; Han, W.; Wang, X. X. Relationship between Oxygen Defects and the Photocatalytic Property of ZnO Nanocrystals in Nafion Membranes. *Langmuir* **2009**, *25*, 1218−1223.

(38) Zheng, Y.; Chen, C.; Zhan, Y.; Lin, X.; Zheng, Q.; Wei, K.; Zhu, J.; Zhu, Y. Luminescence and Photocatalytic Activity of ZnO Nanocrystals: Correlation between Structure and Property. *Inorg. Chem.* **2007**, *46*, 6675−6682.

(39) Liu, S.; Li, C.; Yu, J.; Xiang, Q. Improved Visible-light Photocatalytic Activity of Porous Carbon Self-doped ZnO Nanosheet-assembled Flowers. *CrystEngComm* **2011**, *13*, 2533−2541.

(40) Ahmad, M.; Yingying, S.; Nisar, A.; Sun, H.; Shen, W.; Weie, M.; Zhu, J. Synthesis of Hierarchical Flower-like ZnO Nanostructures and Their Functionalization by Au Nanoparticles for Improved Photocatalytic and High Performance Li-Ion Battery Anodes. *J. Mater. Chem.* **2011**, *21*, 7723−7729.

(41) Ruiz Peralta, M. D. L.; Pal, U.; Zeferino, R. S. Photoluminescence (PL) Quenching and Enhanced Photocatalytic Activity of Au-Decorated ZnO Nanorods Fabricated through Microwave-Assisted Chemical Synthesis. *ACS Appl. Mater. Interfaces* **2012**, *4*, 4807−4816.

(42) Bian, Z. F.; Tachikawa, T.; Kim, W.; Choi, W.; Majima, T. Superior Electron Transport and Photocatalytic Abilities of Metal-Nanoparticle-Loaded TiO_2 Superstructures. *J. Phys. Chem. C* **2012**, *116*, 25444−25453.

(43) Morales-Flores, N.; Pal, U.; Mora, E. S. Photocatalytic Behavior of ZnO and Pt-Incorporated ZnO Nanoparticles in Phenol Degradation. *Appl. Catal., A* **2011**, *394*, 269−275.

(44) Lang, X.; Chen, X.; Zhao, J. Heterogeneous Visible Light Photocatalysis for Selective Organic Transformations. *Chem. Soc. Rev.* **2014**, *43*, 473−486.

(45) Ong, W. L.; Natarajan, S.; Kloostrab, B.; Ho, G. W. Metal Nanoparticle-Loaded Hierarchically Assembled ZnO Nanoflakes for Enhanced Photocatalytic Performance. *Nanoscale* **2013**, *5*, 5568−5575.

(46) Ma, X.; Dai, Y.; Yu, L.; Huang, B. New Basic Insights into the Low Hot Electron Injection Efficiency of Gold-Nanoparticle-Photosensitized Titanium Dioxide. *ACS Appl. Mater. Interfaces* **2014**, *6*, 12388−12394.

(47) Wu, M.; Chen, W. J.; Shen, Y. H.; Huang, F. Z.; Li, C. H.; Li, S. K. In Situ Growth of Matchlike ZnO/Au Plasmonic Heterostructure for Enhanced Photoelectrochemical Water Splitting. *ACS Appl. Mater. Interfaces* **2014**, *6*, 15052−15060.

(48) Ghosh, A.; Juluri, R. R.; Guha, P.; Sathyavathi, R.; Dash, A.; Jena, B. K.; Satyam, P. V. Study of Faceted Au Nanoparticle Capped ZnO Nanowires: Antireflection, Surface Enhanced Raman Spectroscopy and Photoluminescence Aspects. *J. Phys. D: Appl. Phys.* **2015**, *48*, No. 055303.

(49) Wu, Y.; Yang, P. Direct Observation of Vapor-Liquid-Solid Nanowire Growth. *J. Am. Chem. Soc.* **2001**, *123*, 3165−3166.

(50) Chen, X. L.; Lan, Y. C.; Li, J. Y.; Cao, Y. G.; He, M. Radial Growth Dynamics of Nanowires. *J. Cryst. Growth* **2001**, *222*, 586−590.

(51) Gao, T.; Wang, T. Catalyst-Assisted Vapor-Liquid-Solid Growth of Single-Crystal CdS Nanobelts and Their Luminescence Properties. *J. Phys. Chem. B* **2004**, *108*, 20045−20049.

(52) Huang, M. H.; Wu, Y.; Feick, H.; Tran, N.; Weber, E.; Yang, P. Catalytic Growth of Zinc Oxide Nanowires by Vapor Transport. *Adv. Mater.* **2001**, *13*, 113−116.

(53) Kim, D. S.; Scholz, R.; Gosele, U.; Zacharias, M. Gold at the Root or at the Tip of ZnO Nanowires: A Model. *Small* **2008**, *4*, 1615−1619.

(54) Laudise, R. A.; Ballman, A. A. Hydrothermal Synthesis of Zinc Oxide and Zinc Sulfide. *J. Phys. Chem.* **1960**, *64*, 688−691.

(55) Kar, A.; Low, K.; Oye, M.; Stroscio, M. A.; Dutta, M.; Nicholls, A.; Meyyappan, M. Investigation of Nucleation Mechanism and Tapering Observed in ZnO Nanowire Growth by Carbothermal Reduction Technique. *Nanoscale Res. Lett.* **2011**, *6*, 1−9.

(56) Mohammad, S. N. Analysis of the Vapor-Liquid-Solid Mechanism for Nanowire Growth and a Model for this Mechanism. *Nano Lett.* **2008**, *8*, 1532−1538.

(57) Woll, C. The Chemistry and Physics of Zinc Oxide Surfaces. *Prog. Surf. Sci.* **2007**, *82*, 55−120.

(58) Zhu, Z.; Chen, T. L.; Gu, Y.; Warren, J.; Osgood, R. M. Zinc Oxide Nanowires Grown by Vapor-Phase Transport Using Selected Metal Catalysts: A Comparative Study. *Chem. Mater.* **2005**, *17*, 4227−4234.

(59) Kong, Y. C.; Yu, D. P.; Zhang, B.; Fang, W.; Feng, S. Q. Ultraviolet-Emitting ZnO Nanowires Synthesized by a Physical Vapor Deposition Approach. *Appl. Phys. Lett.* **2001**, *78*, 407−409.

(60) Lin, B.; Fu, Z.; Jia, Y. Green Luminescent Center in Undoped Zinc Oxide Films Deposited on Silicon Substrates. *Appl. Phys. Lett.* **2001**, *79*, 943−945.

(61) Vanheusden, K.; Warren, W. L.; Seager, C. H.; Tallant, D. R.; Voigt, J. A. Mechanisms Behind Green Photoluminescence in ZnO Phosphor Powders. *J. Appl. Phys.* **1996**, *79*, 7983−7990.

(62) Jiao, Y.; Zhu, H. J.; Zhou, M. J.; Wang, X. F.; Li, Q. Suppression of Green Emission in ZnO Nanorods—A Discussion on Surface and Interior Structural Quality Manipulation. *J. Phys. Chem. C* **2010**, *114*, 208−211.

(63) Mahalingam, T.; Lee, Y. M.; Park, K. H.; Lee, S.; Ahn, Y.; Park, G. Y.; Koh, K. H. Low Temperature Wet Chemical Synthesis of Good Optical Quality Vertically Aligned Crystalline ZnO Nanorods. *Nanotechnology* **2007**, *18*, No. 035606.

(64) Wang, Y. G.; Lau, S. P.; Zhang, X. H.; Hng, H. H.; Lee, H. W.; Yu, S. F.; Tay, B. K. Enhancement of Near-Band-Edge Photoluminescence from ZnO Films by Face-to-Face Annealing. *J. Cryst. Growth* **2003**, *259*, 335−342.

(65) Leelavathi, A.; Madrasa, G.; Ravishankar, N. Origin of Enhanced Photocatalytic Activity and Photoconduction in High Aspect Ratio ZnO Nanorods. *Phys. Chem. Chem. Phys.* **2013**, *15*, 10795−10802.

(66) Samantara, A. K.; Sahu, S. C.; Bag, B.; Jena, B.; Jena, B. K. Photoelectrocatalytic Oxidation of NADH by Visible Light Driven Plasmonic Nanocomposites. *J. Mater. Chem. A* **2014**, *2*, 12677−12680.

(67) Leng, W. H.; Zhang, Z.; Zhang, J. Q.; Cao, C. N. Investigation of the Kinetics of a TiO_2 Photoelectrocatalytic Reaction Involving Charge Transfer and Recombination through Surface States by Electrochemical Impedance Spectroscopy. *J. Phys. Chem. B* **2005**, *109*, 15008−15023.

(68) Bell, N. J.; Ng, Y. H.; Du, A.; Coster, H.; Smith, S. C.; Amal, R. Understanding the Enhancement in Photoelectrochemical Properties of Photocatalytically Prepared TiO_2-Reduced Graphene Oxide Composite. *J. Phys. Chem. C* **2011**, *115*, 6004−6009.

(69) Jiang, J.; Zhang, X.; Sun, P.; Zhang, L. ZnO/BiOI Heterostructures: Photoinduced Charge-Transfer Property and Enhanced Visible-Light Photocatalytic Activity. *J. Phys. Chem. C* **2011**, *115*, 20555−20564.

(70) Pyne, S.; Sahoo, G. P.; Bhui, D. K.; Bar, H.; Sarkar, P.; Samanta, S.; Maity, A.; Misra, A. Enhanced Photocatalytic Activity of Metal Coated ZnO Nanowires. *Spectrochim. Acta, Part A* **2012**, *93*, 100−105.